AGU PUBLICATIONS

Geophysical Research Letters

RESEARCH LETTER
10.1002/2016GL070403

Key Points:
- MESSENGER's low-altitude images reveal Mercury's ice-bearing polar deposits in high resolution
- All deposits imaged appear young, with low-reflectance surfaces and well-defined boundaries
- Brightness variations provide evidence for multiple volatile organic compounds in the deposits

Supporting Information:
- Supporting Information S1
- Table S1

Correspondence to:
N. L. Chabot,
nancy.chabot@jhuapl.edu

Citation:
Chabot, N. L., C. M. Ernst, D. A. Paige, H. Nair, B. W. Denevi, D. T. Blewett, S. L. Murchie, A. N. Deutsch, J. W. Head, and S. C. Solomon (2016), Imaging Mercury's polar deposits during MESSENGER's low-altitude campaign, *Geophys. Res. Lett.*, *43*, 9461–9468, doi:10.1002/2016GL070403.

Received 11 JUL 2016
Accepted 21 AUG 2016
Accepted article online 23 AUG 2016
Published online 17 SEP 2016

Imaging Mercury's polar deposits during MESSENGER's low-altitude campaign

Nancy L. Chabot[1], Carolyn M. Ernst[1], David A. Paige[2], Hari Nair[1], Brett W. Denevi[1], David T. Blewett[1], Scott L. Murchie[1], Ariel N. Deutsch[3], James W. Head[3], and Sean C. Solomon[4,5]

[1]The Johns Hopkins University Applied Physics Laboratory, Laurel, Maryland, USA, [2]Department of Earth, Planetary, and Space Sciences, University of California, Los Angeles, California, USA, [3]Department of Earth, Environmental and Planetary Sciences, Brown University, Providence, Rhode Island, USA, [4]Lamont-Doherty Earth Observatory, Columbia University, Palisades, New York, USA, [5]Department of Terrestrial Magnetism, Carnegie Institution of Washington, Washington, District of Columbia, USA

Abstract Images obtained during the low-altitude campaign in the final year of the MErcury Surface, Space ENvironment, GEochemistry, and Ranging (MESSENGER) mission provide the highest-spatial-resolution views of Mercury's polar deposits. Images for distinct areas of permanent shadow within 35 north polar craters were successfully captured during the campaign. All of these regions of permanent shadow were found to have low-reflectance surfaces with well-defined boundaries. Additionally, brightness variations across the deposits correlate with variations in the biannual maximum surface temperature across the permanently shadowed regions, supporting the conclusion that multiple volatile organic compounds are contained in Mercury's polar deposits, in addition to water ice. A recent large impact event or ongoing bombardment by micrometeoroids could deliver water as well as many volatile organic compounds to Mercury. Either scenario is consistent with the distinctive reflectance properties and well-defined boundaries of Mercury's polar deposits and the presence of volatiles in all available cold traps.

1. Introduction

Multiple data sets provide evidence that water ice is present in permanently shadowed regions near Mercury's poles. Earth-based radar images revealed materials that are highly reflective at radar wavelengths and have properties consistent with ice-rich deposits [*Slade et al.*, 1992; *Harmon and Slade*, 1992; *Butler et al.*, 1993; *Harmon et al.*, 1994, 2001, 2011]. Imaging and topography data sets identified regions of permanent shadow [*Chabot et al.*, 2012, 2013; *Deutsch et al.*, 2016a]. Thermal models derived from measured topography indicated that temperatures could sustain surface and near-surface water ice in these regions [*Paige et al.*, 2013]. Neutron spectrometry measurements detected enhanced hydrogen in Mercury's north polar region [*Lawrence et al.*, 2013]. Additionally, visible and near-infrared measurements have shown high- and low-reflectance surfaces on the polar deposits [*Neumann et al.*, 2013; *Chabot et al.*, 2014]. The high-reflectance values are consistent with the presence of surficial water ice, but the low-reflectance surfaces require a different explanation.

Both multi-wavelength radar observations [*Harmon et al.*, 2011] and early thermal models [*Vasavada et al.*, 1999] indicated that in many locations near Mercury's poles a thin cover of material likely serves to insulate the water ice and maintain maximum diurnal temperatures that are sufficiently low for the long-term preservation of ice. However, prior to observations by the MErcury Surface, Space ENvironment, GEochemistry, and Ranging (MESSENGER) spacecraft, regolith was generally thought to be the material that insulated the water ice in these regions. Given that the surface reflectance is about half that of surrounding areas [*Neumann et al.*, 2013] and that the low-reflectance deposits occur in locations where water ice is stable only in the shallow subsurface, the cover has been interpreted to be a ~10-cm-thick lag deposit composed of volatile organic-rich material [*Paige et al.*, 2013]. A wide range of volatile organic compounds found in primitive meteorites are stable to higher temperatures than water ice [*Zhang and Paige*, 2009, 2010], consistent with the accumulation of such materials over water ice as the mechanism to produce low-reflectance surfaces. MESSENGER visible-wavelength images of polar deposits revealed that the low-reflectance surfaces have sharp boundaries, but those initial images were limited in resolving other surface morphological details [*Chabot et al.*, 2014].

During the last year of its orbital operations, the MESSENGER spacecraft acquired data at lower periapsis altitudes than possible earlier in the mission, enabling the acquisition of higher-spatial-resolution data sets.

Here we present the results from MESSENGER's low-altitude campaign to image the ice-bearing north polar deposits within Mercury's permanently shadowed craters. The images reveal new details of Mercury's low-reflectance polar deposits and have implications for their source and evolution.

2. Low-Altitude Campaign to Image Polar Deposits

Although Mercury's polar deposits never receive direct sunlight, observations with MESSENGER's Mercury Dual Imaging System (MDIS) have resolved the surfaces within permanently shadowed regions [*Chabot et al*., 2014], which are illuminated by low levels of light scattered by neighboring crater walls and other topographic features. Such observations have been achieved by using the MDIS wide-angle camera (WAC) broadband filter, which has a central wavelength of 700 nm and a bandpass of 600 nm [*Hawkins et al*., 2007]. However, to resolve features within the low-light areas of permanent shadow, exposure times are such that any sunlit portion of the surface contained within the image field of view is highly saturated. The WAC images that are most successful for this type of observation have the shadowed region of interest positioned along the CCD read-out edge, avoiding artifacts due to read-out smear from saturated portions of the scene. Even with shadowed regions optimally positioned in the WAC field of view, the ability of such images to resolve shadowed surfaces is highly dependent on the overall illumination conditions that determine whether sufficient light is scattered into the region. Similar imaging efforts by the Lunar Reconnaissance Orbiter Camera have revealed the surfaces within permanently shadowed regions on the Moon [*Speyerer and Robinson*, 2013; *Koeber et al*., 2014].

Throughout MESSENGER's mission, the spacecraft's orbit was highly eccentric, with a maximum altitude of 10,000–15,000 km over Mercury's south polar region but passing considerably lower over the north polar region. During the first 3 years of the orbital mission, the minimum spacecraft altitude was not permitted to drop below 200 km, but during the final year of the mission, lower periapsis altitudes were designed to enable measurements by MESSENGER's instruments at theretofore unprecedented spatial resolution [*McAdams et al*., 2015]. One investigation implemented to take advantage of this opportunity was MDIS's "low-altitude polar deposits campaign," with the goal of resolving the surfaces of Mercury's permanently shadowed polar deposits in greater detail than was previously possible. From a map of shadowed craters that host radar-bright deposits [*Chabot et al*., 2013], specific craters were targeted for broadband-filter imaging with exposure times of 20–80 ms, and repeat coverage was planned to maximize opportunities for acquiring images with favorable illumination conditions and optimal positioning of the WAC field of view. Coverage limitations were imposed by the times and locations when the spacecraft was at low altitudes over the sunlit surface.

With low altitude defined to be altitudes $<$250 km, MDIS acquired 717 images for the low-altitude polar deposits campaign from 10 June 2014 to 13 April 2015. Of those images, 402 were successful at revealing features within permanently shadowed craters and subsequently were divided into groups on the basis of geographic location. All of the images within a group were inspected together, to select the best coverage for as many distinct craters as possible. This approach led to the identification of 77 images that revealed best the shadowed surfaces within 35 distinct craters. The footprints of these images are shown in Figure 1, along with radar-bright [*Harmon et al*., 2011] and permanently shadowed [*Deutsch et al*., 2016a] regions. The 77 images have pixel scales from 24 to 96 m, acquired at altitudes from 67 to 250 km, with additional details given in Table S1 in the supporting information. Though we focus on these 77 images, the other successful low-altitude WAC broadband images provide different views under a range of illumination conditions and support the conclusions reached in this study. While the images from the low-altitude campaign shown in Figure 1 cover a range of longitudes, imaging at high resolution Mercury's northernmost craters that host radar-bright deposits was not possible during this campaign because periapsis latitudes ranged from ~60° to 70°N during the spacecraft's last year of operations.

3. Imaging Results and Observations

Overall, images from MESSENGER's low-altitude polar deposits campaign lead to three main observations:

1. The low-reflectance deposits have well-defined boundaries, even in the highest-resolution images obtained by MESSENGER.
2. The low-reflectance deposits do not have uniform brightness across a single deposit.

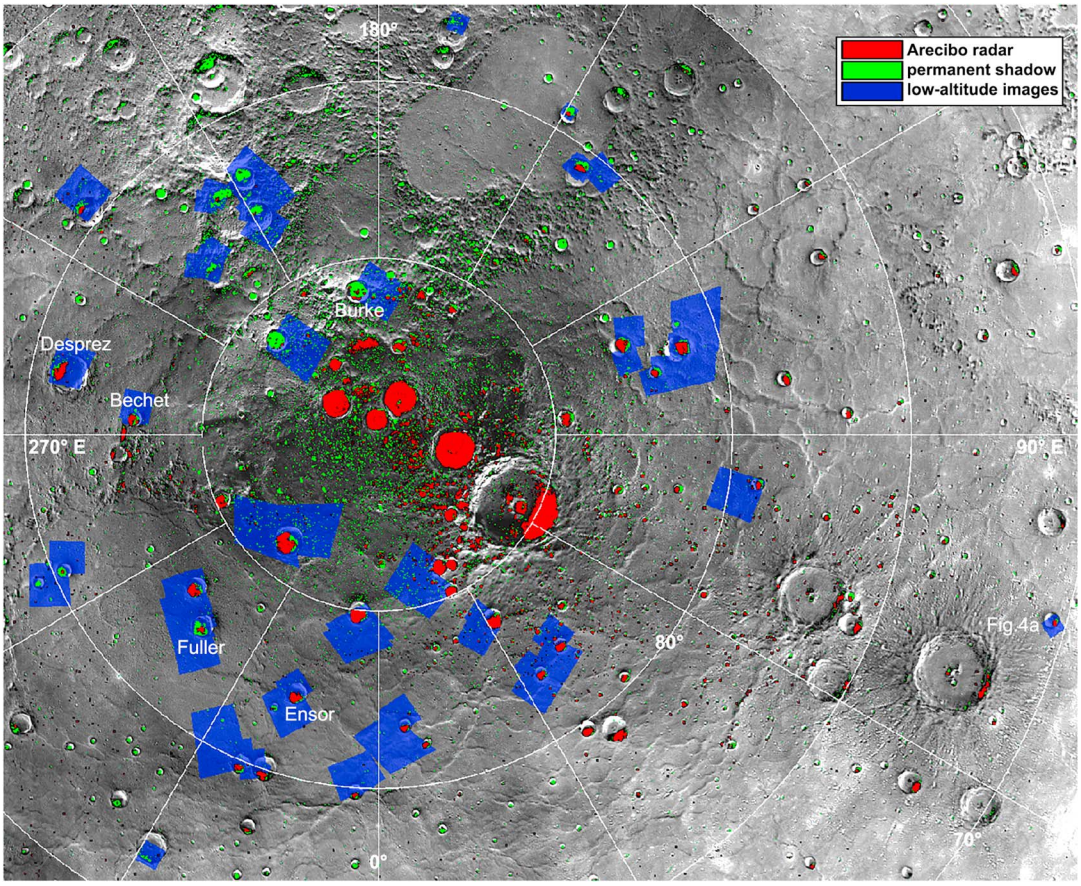

Figure 1. Locations of images from MESSENGER's low-altitude polar deposits campaign that were identified in this study as revealing best the surfaces of the polar deposits. Blue: low-altitude WAC broadband image footprints. Red: regions with high radar backscatter [*Harmon et al*., 2011]. Green: regions of permanent shadow, modeled from Mercury's topography [*Deutsch et al*., 2016a]. Craters shown in Figures 2–4 are labeled.

3. All of the 35 craters imaged during MESSENGER's low-altitude polar deposits campaign contain low-reflectance surfaces that collocate with regions of permanent shadow, even if such craters lack extensive radar-bright regions.

In this section, we discuss each of these observations in more detail, beginning with a detailed look at the crater Desprez, shown in Figure 2.

Desprez is one of the largest permanently shadowed craters imaged during the low-altitude campaign. The location of the sharp boundary of the low-reflectance surface in Desprez agrees well with the region modeled as permanently shadowed, as determined from a digital elevation model (DEM) derived from measurements by MESSENGER's Mercury Laser Altimeter (MLA) [*Deutsch et al*., 2016a]. With this same MLA-derived DEM, thermal models were run for Mercury's north polar region at a spatial scale of 1 km, following the approach of *Paige et al*. [2013]. Because the models for the permanently shadowed regions and the thermal conditions are both based on the same DEM, the results of the two are necessarily in agreement. Figure 2b shows locations within Desprez with modeled biannual maximum surface temperatures <250 K, which correspond to the locations that experience permanent shadow in this crater. As noted previously from lower resolution MDIS images [*Chabot et al*., 2014], the locations and boundaries of the low-reflectance deposits are highly consistent with the locations of permanent shadow, the thermal stability of water ice covered by a ~10-cm-thick insulating layer [*Paige et al*., 2013], and low MLA reflectance values [*Neumann et al*., 2013]. These inferences continue to be supported by the low-altitude images described in this study.

An important advance achieved by the low-altitude, higher-resolution images is that they enable the identification of new details within the polar deposits. Figure 2c shows that the low-reflectance region within Desprez is not featureless but rather exhibits brightness variations across the deposit. Small craters are also

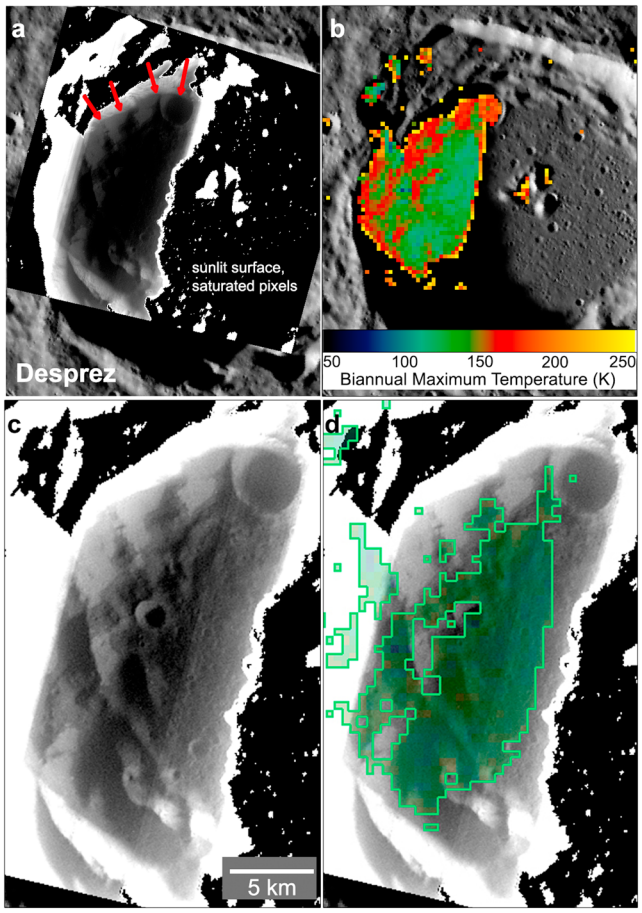

Figure 2. Desprez crater (47 km diameter; centered at 81.1°N, 258.7°E); stereographic projection about the north pole, with 180°E to the top. (a) WAC broadband image (EW1068404967B, 69 m/pixel) highlighting the well-defined boundary of the low-reflectance surface (red arrows). Sunlit regions that were saturated in the image are shown in black. (b) Thermal model of the biannual maximum surface temperature, filtered to display values that are <250 K, corresponding to the permanently shadowed region of Desprez. (c) Expanded view of the image in Figure 2a, but with a different stretch to reveal pixel brightness variations across the region. (d) Locations in green are modeled to have biannual maximum surface temperatures <150 K.

visible on the low-reflectance deposit, but these small craters do not appear to be related to the brightness variations observed. Instead, the brightness variations in Desprez show a resemblance to the map of modeled biannual maximum surface temperature, with pixel value differences of approximately 15% that correspond to these variations. In Figure 2d, regions that have a modeled maximum surface temperature <150 K are outlined and map out a pattern similar to that observed for the darker portions of the permanently shadowed region. Control of surface reflectance variations by temperature could be the result of multiple volatile species that differ in reflectance and are stable to different maximum temperatures.

However, interpreting even relative surface reflectance properties from a WAC broadband image is not straightforward, as regions may appear dark in the images from having surfaces with inherently lower reflectance, from being doubly shadowed (not receiving any direct or singly reflected indirect illumination [*Speyerer and Robinson*, 2013]) by the topography, or from receiving different amounts of indirect illumination. Additionally, variations from features on a scale smaller than the pixel scale of the image, such as surface roughness variations [*Davidsson and Rickman*, 2014], could also influence the thermal conditions and hence the stability of different volatile compounds, potentially resulting in variations in surface reflectance across the images. The illumination in each of the WAC broadband images is complicated, with sunlight scattered into the scene from multiple surfaces, directions, and angles. Modeling of the illumination conditions at the acquisition time of each image is required to determine absolute reflectance values for the surfaces and also would aid in the interpretation of brightness variations caused by shadowing or illumination differences across the scene.

Examples of high-resolution images of polar deposits in four other craters (Ensor, Burke, Fuller, and Bechet) are shown in Figure 3, and a view of the shadowed surface within the lowest-latitude crater successfully imaged by this low-altitude campaign is shown in Figure 4a. All five of these craters show low-reflectance surfaces with well-defined boundaries. The low-altitude images enable the boundaries of the low-reflectance surfaces to be evaluated at a finer spatial scale than previously possible. Figure 4b shows transects of relative brightness values measured across the low-reflectance boundaries in three of these craters. Transects were determined by averaging areas ~400–1500 m in width over lengths of at least 2 km. These particular craters were selected for this analysis because it was possible to acquire transects that largely avoided steep crater walls, which often show increasing brightness with decreasing distance to the crater rim due to the scattered

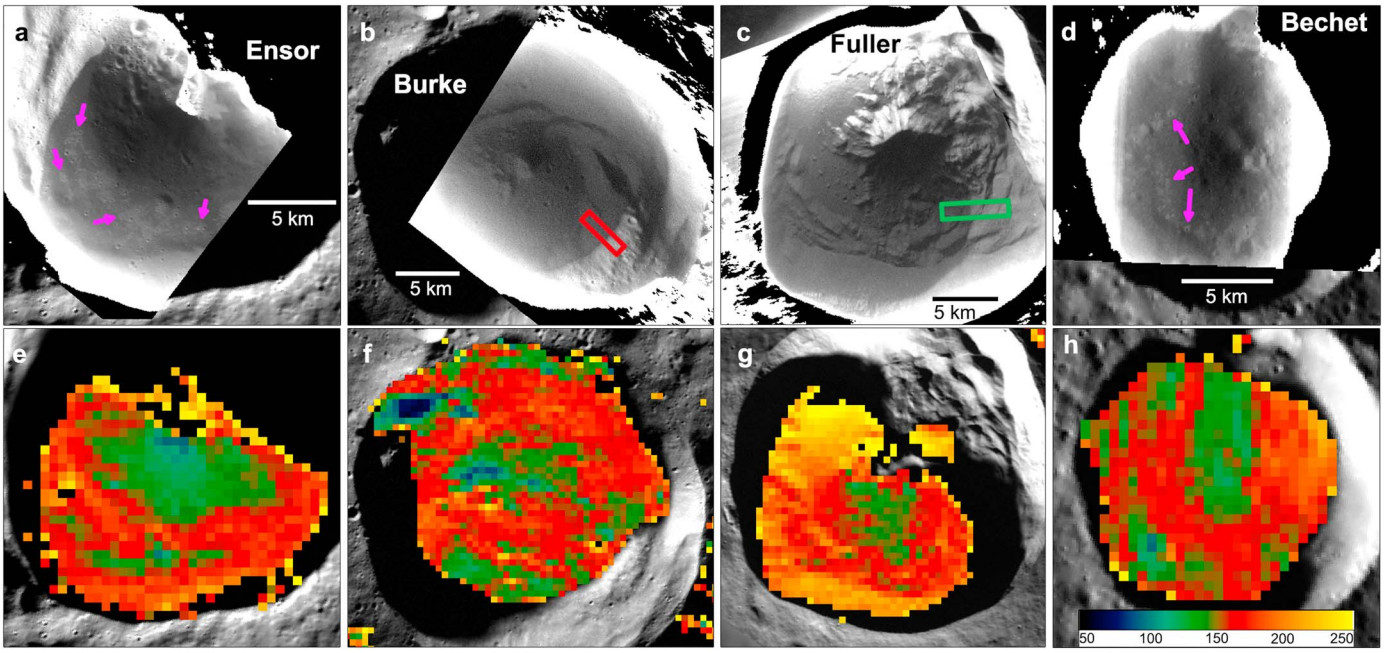

Figure 3. Low-altitude WAC broadband images of (a) Ensor (25 km diameter; 82.3°N, 342.5°E; EW1051458815B, 37 m/pixel), (b) Burke (29 km diameter; 85.9°N, 188.4°E; EW1058852260B, 44 m/pixel), (c) Fuller (27 km diameter; 82.6°N, 317.3°E; EW1047206595B, 43 m/pixel), and (d) Bechet (18 km diameter; 83.1°N, 266.3°E; EW1068077244, 58 m/pixel). Pink arrows identify examples of small-scale variations in brightness. Red and green rectangles denote the locations of the transects in Figure 4b. (e–h) Models of biannual maximum surface temperature in K for each crater above, for locations <250 K. All images are in stereographic projection about the north pole, with 180°E to the top.

light that illuminates the scene. As may be seen in Figure 4b, the well-defined boundaries of the low-reflectance surfaces display a transition zone approximately 400 m wide between the permanently shadowed, low-reflectance deposit and the regolith that receives direct sunlight. Though the specific transect acquired for the lowest-latitude crater displays a slightly narrower transition zone, and the transition zone of Burke is measured to be slightly wider, all three transects plotted in Figure 4b are generally similar, given the complicated illumination conditions of the images. The ~400-m-wide zone of intermediate

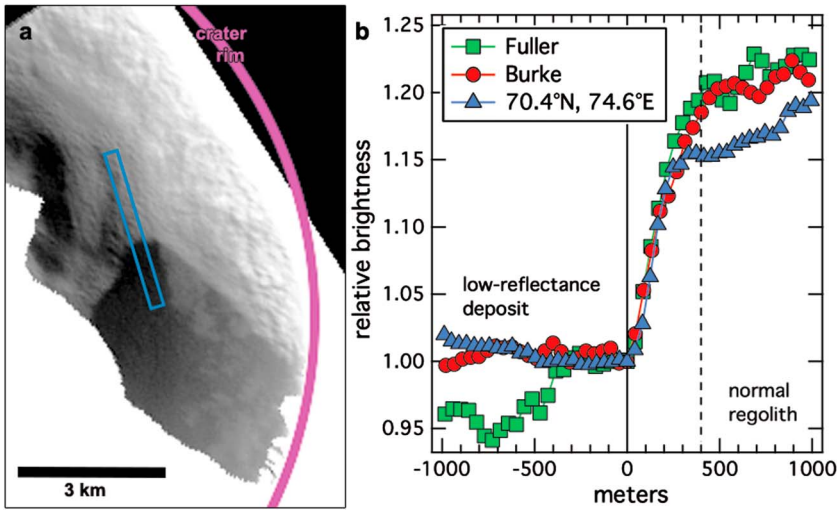

Figure 4. (a) WAC broadband image of the permanently shadowed crater at the lowest latitude imaged during the low-altitude campaign (18 km diameter; 70.4°N, 74.6°E; EW1059620770, 41 m/pixel). The crater rim is outlined in pink. The blue rectangle denotes the location of the transect in Figure 4b. Stereographic projection about the north pole, with 180°E to the top. (b) Transects of relative pixel brightness across the boundaries of the low-reflectance deposits in Fuller, Burke, and the crater shown in Figure 4a, normalized to unity at the boundary edge.

values could be due to mixing between the low-reflectance material and regolith, or it could be due to variations in the amount of sunlit and permanently shadowed areas in this region on a scale smaller than the spatial resolution of the images.

The four craters shown in Figure 3 also display some variations in surface brightness within the low-reflectance regions, but these variations are not as clearly correlated with the biannual maximum surface temperature as is Desprez (Figure 2). Nonetheless, the modeled ranges of maximum surface temperatures experienced within the four craters of Figure 3 are comparable with that of Desprez, and there is some resemblance between the surface brightness and predicted thermal patterns. For example, the colder region near the center of Ensor appears to be slightly darker in the WAC broadband image, and the darker curved patterns observed in the WAC broadband image of Burke resemble features in the thermal model for this crater. In contrast, though biannual maximum surface temperature variations are predicted in Fuller, the low-reflectance surface in this crater appears highly uniform in the WAC broadband image. Ensor and Bechet also have small-scale variations in brightness (pink arrows in Figure 3) that look as if they could be related to small impact craters that have disturbed the surfaces of the low-reflectance regions. In general, the considerable difference between the 1-km spatial scale of the thermal model and the tens-of-meters pixel scale of the low-altitude images makes interpretation challenging. Desprez is one of the largest permanently shadowed craters imaged during MESSENGER's low-altitude campaign, and thus it may host thermal variations on a larger scale, making it easier for the 1-km scale thermal model to resolve such variations more readily than those within the smaller craters depicted in Figure 3.

A final observation that we note from MDIS's low-altitude polar deposits campaign is that all of the 35 distinct permanently shadowed craters imaged successfully during the campaign were observed to have low-reflectance surfaces. In all cases, the low-reflectance surfaces display well-defined boundaries that consistently align with regions of permanent shadow. In contrast, not all of these 35 craters host extensive radar-bright regions. As one example, Burke crater, shown in Figure 3, shows a low-reflectance surface that covers much of the crater's interior, yet this crater lacks an extensive radar-bright deposit, as seen in Figure 1. The low-reflectance surfaces observed in craters that lack extensive radar-bright deposits appear similar to the low-reflectance surfaces within craters that do host extensive radar-bright deposits. These similarities are consistent with the notion that the lack of radar-bright features associated with some permanently shadowed craters is the result of limitations to the radar imaging data rather than an absence of water ice in these craters. However, as discussed by *Deutsch et al*. [2016a], modeling the Arecibo radar viewing opportunities suggests that limited radar coverage cannot account for the lack of extensive radar-bright deposits in these craters. Nevertheless, other factors, such as the sensitivity of the radar observations during specific viewing opportunities or the approach used to combine radar observations from multiple nights into a single image, could contribute to the lack of extensive radar-bright deposits within some craters in a composite view such as Figure 1.

4. Conclusions and Implications for Mercury's Polar Deposits

Two of the main observations from the low-altitude polar deposits campaign provide evidence that the delivery of volatiles to Mercury either occurred in the geologically recent past or is continuing through an ongoing process. First, the observation that the low-reflectance boundaries are well defined but also have an approximately ~400-m-wide transition zone is a new result enabled by the finer spatial scale of the low-altitude images. The nature of the transition zone, whether due to mixing or to small-scale variations in the amount of shadow, is not currently known. Models of the rates associated with lateral mixing by impacts could place a maximum age constraint on the low-reflectance surfaces from this newly determined width for the zone with intermediate reflectance properties. Regolith gardening models suggest that 20 cm of regolith would cover Mercury's polar deposits in $<$50 My [*Crider and Killen*, 2005], and the low-altitude images reveal low-reflectance deposits that are not completely buried by regolith but rather maintain well-defined boundaries, supporting the conclusion that the deposits are relatively young.

Second, the fact that every permanently shadowed crater imaged during MESSENGER's low-altitude imaging campaign hosts low-reflectance material supports the notion that all of Mercury's available polar cold traps are occupied by volatiles. This observation suggests that Mercury's polar volatiles were emplaced more recently than the formation time of any of the polar cold traps, also supporting the conclusion that the polar deposits are relatively young and providing a potential means to estimate a maximum age [*Deutsch et al*., 2016b].

The third main observation from the low-altitude images supports the notion that Mercury's polar water ice and volatiles are delivered during impacts from comets, asteroids, and/or micrometeoroids. The agreement between the brightness variations observed within Desprez and the modeled biannual maximum surface temperature is consistent with the presence of multiple low-reflectance volatiles exposed on the permanently shadowed surface within this crater. There are a large number of organic compounds that are each stable as solids up to a temperature higher than the maximum for water ice but only for temperatures $<$250 K, and primitive objects, such as comets, asteroids, or micrometeoroids, are thought to contain a wide range of such volatile compounds [*Zhang and Paige*, 2009, 2010]. In particular, Desprez shows evidence for different surface volatiles in areas with maximum temperatures $<$150 K than are present where maximum temperatures range between 150 and 250 K. Many carboxylic acids, for instance, are stable as solids to temperatures between 150 and 250 K, whereas many aromatic hydrocarbons are stable as solids only to temperatures $<$150 K [*Zhang and Paige*, 2009, 2010], and both of these classes of compounds are found in primitive meteorites [*Botta and Bada*, 2002].

Thus, the observations from the low-altitude images support the conclusion that a substantial source of Mercury's polar deposits is either the impact onto Mercury's surface of a large comet or volatile-rich asteroid within the last few tens of millions of years or the continuous and ongoing delivery of primitive micrometeoroids.

More work is needed to investigate the survival and retention potential of water and other volatiles during a large impact on Mercury, as has been done for the Moon [*Ong et al*., 2010; *Stewart et al*., 2011; *Prem et al*., 2015]. Modeling shows that a single comet impact would lead to the capture of water molecules in cold traps at both lunar polar regions [*Stewart et al*., 2011]. Thus, the extensive radar-bright deposits in permanently shadowed regions near both Mercury's north and south [*Harmon et al*., 2011; *Chabot et al*., 2012] poles could be consistent with a large, recent impact event as the source of Mercury's water ice. The higher velocity associated with impacts on Mercury [*Le Feuvre and Wieczorek*, 2008] may decrease the retention of water and other volatiles [*Ong et al*., 2010], but differences from the Moon such as Mercury's greater surface gravitational acceleration and its different thermal environment may also be important factors in the retention of volatiles. A large recent impact on Mercury would leave a young crater on the surface, and investigations to identify the source crater, such as the study focused on Hokusai crater [*Ernst et al*., 2016], are well motivated by the results from MESSENGER's low-altitude polar deposits campaign.

Alternatively, primitive micrometeoroids could also deliver water and organic compounds to Mercury [*Bruck Syal and Schultz*, 2015], and many more micrometeoroids impact Mercury than the Moon [*Cintala*, 1992; *Borin et al*., 2009, 2016]. Micrometeoroid impacts provide a continuing source of volatiles to Mercury, and hence the observations in this study of distinct reflectance properties, well-defined boundaries, and volatiles in all polar cold traps could be consistent with such a source. However, Earth-based radar studies have provided constraints on the purity of the water ice near Mercury's poles and indicate that polar deposits contain $<$5% silicates by volume [*Butler et al*., 1993] and are at least several meters thick [*Black et al*., 2010]. Producing and preserving such a thick and pure layer of water ice could be difficult if delivered by a continuing source, such as micrometeoroids, instead of an episodic source, such as a recent large impact. New models to investigate the production of Mercury's polar deposits from micrometeoroids, as well as studies to refine the constraints on the purity or depth of the ice deposits, could provide means to evaluate these possibilities.

Finally, though the variations in brightness observed within Desprez are well correlated with the modeled maximum surface temperature, interpretation of the observed variations in surface brightness (or the lack thereof) in other craters is less straightforward. If some of these variations across the low-reflectance deposits are associated with the exposure of material by small impact craters, such an observation is not clearly consistent with the view that the low-reflectance deposits are geologically young, as deduced from their distinctive reflectance properties and well-defined boundaries. Conversely, if it is confirmed that small craters do excavate fresh material in these regions, such a result would provide an important constraint on the timing, depth, or rate of formation of the low-reflectance material. Future studies that apply higher-resolution thermal and illumination models to the specific craters identified here are well suited to address these questions.

Acknowledgments

The MESSENGER project is supported by the NASA Discovery Program under contracts NAS5-97271 to The Johns Hopkins University Applied Physics Laboratory and NASW-00002 to the Carnegie Institution of Washington. Support was also provided by the MESSENGER Participating Scientist Program (NNX07AR64G to D.A. Paige and NNX08AN29G to D.T. Blewett) and NASA Discovery Data Analysis Program grant NNX15AK89G to N.L. Chabot. This research made use of the Integrated Software for Imagers and Spectrometers of the U.S. Geological Survey. All data analyzed in this paper are archived at the NASA Planetary Data System.

References

Black, G. J., D. B. Campbell, and J. K. Harmon (2010), Radar measurements of Mercury's north pole at 70 cm wavelength, *Icarus*, *209*, 224–229, doi:10.1016/j.icarus.2009.10.009.

Borin, P., G. Cremonese, F. Marzari, M. Bruno, and S. Marchi (2009), Statistical analysis of micrometeoroids flux on Mercury, *Astron. Astrophys.*, *503*, 259–264, doi:10.1051/0004-6361/200912080.

Borin, P., G. Cremonese, M. Bruno, and F. Marzari (2016), Asymmetries in the dust flux at Mercury, *Icarus*, *264*, 220–226.

Botta, O., and J. L. Bada (2002), Extraterrestrial organic compounds in meteorites, *Surv. Geophys.*, *23*, 411–467.

Bruck Syal, M., and P. H. Schultz (2015), Impact delivery of water at the Moon and Mercury, *Lunar Planet. Sci.*, *46*, Abstract 1680.

Butler, B. J., D. O. Muhleman, and M. A. Slade (1993), Mercury: Full-disk radar images and the detection and stability of ice at the north pole, *J. Geophys. Res.*, *98*, 15,003–15,023, doi:10.1029/93JE01581.

Chabot, N. L., C. M. Ernst, B. W. Denevi, J. K. Harmon, S. L. Murchie, D. T. Blewett, S. C. Solomon, and E. D. Zhong (2012), Areas of permanent shadow in Mercury's south polar region ascertained by MESSENGER orbital imaging, *Geophys. Res. Lett.*, *39*, L09204, doi:10.1029/2012GL051526.

Chabot, N. L., C. M. Ernst, J. K. Harmon, S. L. Murchie, S. C. Solomon, D. T. Blewett, and B. W. Denevi (2013), Craters hosting radar-bright deposits in Mercury's north polar region: Areas of persistent shadow determined from MESSENGER images, *J. Geophys. Res. Planets*, *118*, 26–36, doi:10.1029/2012JE004172.

Chabot, N. L., et al. (2014), Images of surface volatiles in Mercury's polar craters acquired by the MESSENGER spacecraft, *Geology*, *42*, 1051–1054.

Cintala, M. J. (1992), Impact-induced thermal effects in the lunar and Mercurian regoliths, *J. Geophys. Res.*, *97*, 947–973, doi:10.1029/91JE02207.

Crider, D., and R. M. Killen (2005), Burial rate of Mercury's polar volatile deposits, *Geophys. Res. Lett.*, *32*, L12201, doi:10.1029/2005GL022689.

Davidsson, B. J. R., and H. Rickman (2014), Surface roughness and three-dimensional heat conduction in thermophysical models, *Icarus*, *243*, 58–77.

Deutsch, A. N., N. L. Chabot, E. Mazarico, C. M. Ernst, J. W. Head, G. A. Neumann, and S. C. Solomon (2016a), Comparison of areas in shadow from imaging and altimetry in the north polar region of Mercury and implications for polar ice deposits, *Icarus*, *280*, 158–171, doi:10.1016/j.icarus.2016.06.015.

Deutsch, A. N., J. W. Head, C. I. Fassett, and N. L. Chabot (2016b), Ice deposits at Mercury's north polar region: Host craters provide maximum age, *Lunar Planet. Sci.*, *47*, Abstract 2319.

Ernst, C. M., N. L. Chabot, and O. S. Barnouin (2016), Examining the potential contributions of the Hokusai impact to water ice on Mercury, *Lunar Planet. Sci.*, *47*, Abstract 1374.

Harmon, J. K., and M. A. Slade (1992), Radar mapping of Mercury: Full-disk images and polar anomalies, *Science*, *258*, 640–643, doi:10.1126/science.258.5082.640.

Harmon, J. K., M. A. Slade, R. A. Vélez, A. Crespo, M. J. Dryer, and J. M. Johnson (1994), Radar mapping of Mercury's polar anomalies, *Nature*, *369*, 213–215.

Harmon, J. K., P. J. Perillat, and M. A. Slade (2001), High-resolution radar imaging of Mercury's north pole, *Icarus*, *149*, 1–15.

Harmon, J. K., M. A. Slade, and M. S. Rice (2011), Radar imagery of Mercury's putative polar ice: 1999–2005 Arecibo results, *Icarus*, *211*, 37–50, doi:10.1016/j.icarus.2010.08.007.

Hawkins, S. E., III, et al. (2007), The Mercury Dual Imaging System on the MESSENGER spacecraft, *Space Sci. Rev.*, *131*, 247–338, doi:10.1007/s11214-007-9266-3.

Koeber, S. D., M. S. Robinson, and E. J. Speyerer (2014), LROC observations of permanently shadowed regions on the Moon, *Lunar Planet. Sci.*, *45*, Abstract 2811.

Lawrence, D. J., et al. (2013), Evidence for water ice near Mercury's north pole from MESSENGER Neutron Spectrometer measurements, *Science*, *339*, 292–296, doi:10.1126/science.1229953.

Le Feuvre, M., and M. A. Wieczorek (2008), Nonuniform cratering of the terrestrial planets, *Icarus*, *197*, 291–306.

McAdams, J. V., et al. (2015), Engineering MESSENGER's grand finale at Mercury—The low-altitude hover campaign, paper AAS 15-634 presented at Astrodynamics Specialist Conference, Am. Astronaut. Soc., Vail, Colo., 9–13 Aug.

Neumann, G. A., et al. (2013), Bright and dark polar deposits on Mercury: Evidence for surface volatiles, *Science*, *339*, 296–300, doi:10.1126/science.1229764.

Ong, L., E. I. Asphaug, D. Korycansky, and R. F. Coker (2010), Volatile retention from cometary impacts on the Moon, *Icarus*, *207*, 578–589.

Paige, D. A., M. A. Siegler, J. K. Harmon, G. A. Neumann, E. M. Mazarico, D. E. Smith, M. T. Zuber, E. Harju, M. L. Delitsky, and S. C. Solomon (2013), Thermal stability of volatiles in the north polar region of Mercury, *Science*, *339*, 300–303, doi:10.1126/science.1231106.

Prem, P., N. A. Artemieva, D. B. Goldstein, P. L. Varghese, and L. M. Trafton (2015), Transport of water in a transient impact-generated lunar atmosphere, *Icarus*, *255*, 148–158, doi:10.1016/j.icarus.2014.10.017.

Slade, M. A., B. J. Butler, and D. O. Muhleman (1992), Mercury radar imaging: Evidence for polar ice, *Science*, *258*, 635–640, doi:10.1126/science.258.5082.635.

Speyerer, E. J., and M. S. Robinson (2013), Persistently illuminated regions at the lunar poles: Ideal sites for future exploration, *Icarus*, *222*, 122–136, doi:10.1016/j.icarus.2012.10.010.

Stewart, B. D., E. Pierazzo, D. B. Goldstein, P. L. Varghese, and L. M. Trafton (2011), Simulations of a comet impact on the Moon and associated ice deposition in polar cold traps, *Icarus*, *215*, 1–16.

Vasavada, A. R., D. A. Paige, and S. E. Wood (1999), Near-surface temperatures on Mercury and the Moon and the stability of polar ice deposits, *Icarus*, *141*, 179–193, doi:10.1006/icar.1999.6175.

Zhang, J. A., and D. A. Paige (2009), Cold-trapped organic compounds at the poles of the Moon and Mercury: Implications for origins, *Geophys. Res. Lett.*, *36*, L16203, doi:10.1029/2009GL038614.

Zhang, J. A., and D. A. Paige (2010), Correction to "Cold-trapped organic compounds at the poles of the Moon and Mercury: Implications for origins", *Geophys. Res. Lett.*, *37*, L03203, doi:10.1029/2009GL041806.